Available online at www.sciencedirect.com

ScienceDirect

Journal of Magnesium and Alloys 10 (2022) 756–768

www.elsevier.com/locate/jma

Full Length Article

Corrosion resistance of pulsed laser modified AZ31 Mg alloy surfaces

S. Fajardo*, L. Miguélez, M.A. Arenas, J. de Damborenea, I. Llorente, S. Feliu

Department of Surface Engineering, Corrosion and Durability, National Centre for Metallurgical Research (CENIM-CSIC), Madrid 28040, Spain

Received 11 February 2021; received in revised form 29 September 2021; accepted 29 September 2021
Available online 8 December 2021

Abstract

The effect of laser surface melting on the corrosion resistance of AZ31 Mg alloy in 0.1 M NaCl solution was investigated using different laser processing conditions (energy densities of 14 and 17 J cm^{-2}). Laser treatment induced rough surfaces primarily composed of oxidized species of Mg. XPS analysis revealed that the surface concentration of Al increased significantly as a consequence of LSM. Electrochemical impedance spectroscopy showed that the laser treatment remarkably increased the polarization resistance of the AZ31 Mg alloy and induced a passive-like region of about 100 mV, as determined by potentiodynamic polarization. Analysis of the results obtained provide solid evidence that within the immersion times used in this study, LSM treatment increased the corrosion resistance of AZ31 Mg alloy under open circuit conditions and anodic polarization.

Keywords: Mg alloys; laser surface melting (LSM); Electrochemical impedance; Potentiodynamic polarization; corrosion resistance.

1. Introduction

Among all the metallic materials used for structural applications, magnesium (Mg) alloys have the lowest density (2/3 of aluminum and 1/4 of steel). This makes them very attractive materials for the aerospace and land transportation industries. The lighter weight of a Mg-based vehicle reduces fuel consumption and the emission of greenhouse gasses. For instance, it is estimated that the replacement of multiple components of a car with 72 kg of Mg alloy can provide a weight reduction of 48.5 kg and 19.5 kg and a fuel saving of 0.25 and 0.1 L per 100 km in the cases of steel and aluminum, respectively [1]. More recently, it has been reported that substitution of steel, aluminum and mild steel by magnesium implies a weight reduction of about 62%, 10–41% and 75–81%, respectively [2]. In addition, Mg alloys present a high strength-to-weight ratio, excellent formability, castability, machinability and weldability [3]. Furthermore, the interest in the use of Mg alloys as a material for temporary implants is increasing due to a good combination of mechanical strength, similar elastic modulus to bone, biocompatibility, biodegradability and the ability to promote osteogenesis [4–6]. However, their low resistance to corrosion and wear remains one of the main limitations in the use of Mg alloys for transportation applications [7,8].

Corrosion resistance is commonly associated with the chemical activity of a metal surface and the protective properties of surface films. In the case of Mg alloys, the combination of a high reactivity in aqueous environments and the poor protection provided by the native oxide layer are responsible for their low resistance against corrosion [3,9]. However, it is possible to improve the corrosion resistance of these materials by appropriate surface modification, inducing microstructural and compositional changes in the outermost region of the metal [10]. There are several methods available for surface modification of Mg alloys with the aim of improving their corrosion resistance such as the use of conversion coatings, anodization, sol-gel coatings, ionic implantation, laser surface melting, friction stir processing, chemical passivation, application of organic coatings and plasma electrolytic oxidation [8,11-16]. Among them, laser surface modification and specially laser surface melting (LSM) offer numerous advantages compared to more conventional protection techniques

* Corresponding author.
E-mail address: fajardo@cenim.csic.es (S. Fajardo).

https://doi.org/10.1016/j.jma.2021.09.020

like fast and flexible processing, easy automation, excellent reproducibility and the lack of surface pretreatment necessity [8,17]. Furthermore, LSM is a fast solidification method that can promote the generation of very thin melted surface layers without altering the bulk metal significantly [8]. From a microstructural perspective, the improved corrosion resistance using this method is primarily associated with the formation of fine dendritic grains in the modified region. These microstructural changes may promote the dissolution and redistribution of second phases (i.e. intermetallic particles), hindering the formation of microgalvanic couples thus improving the corrosion resistance of Mg alloys [8,18]. Regarding the oxide surface film modification, even though LSM does not normally induce significant compositional changes in the treated surface, evaporation of any of the alloying elements is possible [8]. For instance, selective evaporation of Mg and Zn in the AZ Mg alloy series would result in an Al enriched surface, enhancing the corrosion resistance of the laser treated regions [6].

The use of different types of laser for LSM treatments, such as excimer lasers or continuous-wave (CW) or long pulsed lasers, result in different solidification microstructures, which leads to different mechanisms of improving corrosion resistance of Mg alloys. Liu et al. [12] and Wang et al. [16] used continuous-wave CO_2 laser (10 kW) to improve the corrosion properties of AM60B and AZ91 Mg alloys, respectively, by changing the microstructure, such as grain refinement, Al element enrichment [12] and homogeneous redistribution of the intermetallic β-$Mg_{17}Al_{12}$ phase in the alloys after treatment. Also, LSM treatment of MEZ alloy (0.5 wt.% Zn, 0.1 wt.% Mn, 0.1 wt.% Zr, 2 wt.% RE, Mg balance) using continuous-wave CO_2 laser (10 kW) enhanced the corrosion resistance attributed to the combined influence of grain refinement, dissolution of intermetallic phases, and the presence of rare earth elements in the extended solid solution [19]. Abbas et al. [20] studied laser surface melting of AZ31, AZ61 and WE43 Mg alloys with a 2 kW continuous-wave CO_2 laser beam and observed an improvement of 30%, 66% and 87% improvement in corrosion resistance for AZ31, AZ61 and WE43 Mg alloys, respectively. In agreement with Liu et al. [12] and Wang et al. [16], this was attributed to a refinement in the microstructure of the alloy, and a more homogenous redistribution of the β-phase. However, Banerjee et al. [21] indicated that the corrosion resistance of ZE41 Mg alloy was not significantly improved by an Nd:YAG laser operating in a continuous wave mode, although microstructural refinement was achieved. This is due to absence of beneficial alloying elements such as Al.

Studies reported by Taltavull et al. [18] on the high power diode laser (HPDL) processing indicate that changes in corrosion resistance depended on processing operating parameters as well as on the surface roughness. In summary, enhanced corrosion resistance was observed at increasing laser beam power and decreasing laser scanning speed. Coy et al. [10] investigated the effect LSM on the microstructure and corrosion behavior of AZ91D Mg alloy using an excimer laser. Improvement of the corrosion resistance of the alloy was associated with the large dissolution of intermetallic phases and the enrichment of aluminum within the highly homogeneous and refined melted microstructure. Khalfaoui et al. [22] observed improved corrosion behavior of a LSM treated ZE41 Mg alloy using an excimer KrF laser. The melted Mg-alloy presented a homogenous distribution of the alloying elements in the magnesium matrix. In contrast, Dubé et al. [23] reported that the corrosion of AZ91D and AM60B Mg alloys melted with the use of pulsed Nd:YAG laser was not significantly reduced even though the microstructure of both alloys was refined.

In addition to the laser surface melting technique, electron beam processing (EBP) is one of the most effective way to improve the corrosion resistance of magnesium alloys [24,25]. EBP exhibits essential advantages over laser and ion beams with its great efficiency, simplicity, and reliability [25]. K. Zhang et al. [26] used a high-current pulsed electron beam (HCPEB) to process as-cast WE43 Mg alloy, and the disappearance of second phase, the formation of homogeneous dispersed β' nano-precipitates and the chemically homogenized melted layer improved its corrosion resistance in vitro. Recently, Liu et al. [27] found that Mg-4Sm alloy treated by HCPEB shows the lowest corrosion current density among all samples, which can be attributed to the homogenous microstructure and composition with fewer defects in the surface layer after repeated melting and rapid solidification. Finally, Lee et al. [28] observed that selective evaporation of Mg induced by large pulsed electron beam (LPEB) irradiation led to the formation of an Al-enriched re-solidified layer with nano-grained structure consisting of $Mg_{3.1}Al_{0.9}$ metastable phase, promoting a decrease in the corrosion rate of AZ31B Mg alloy in 3.5% NaCl solution.

In a previous work, it was found that an Al enrichment (of about 0.5 and 0.8 wt.%) within a surface layer of approximately 10 μm substantially improved the corrosion resistance on a AZ31 Mg alloy manufactured by twin-cast rolling method [29]. The present paper aims to further explore the effect of LSM using a nanosecond low power Nd:YAG laser under different laser processing conditions on the Al enrichment of AZ31 Mg alloy and its corrosion behavior in 0.1 M NaCl solution. Even though laser treatment may also induce microstructural changes in the outermost region of the test specimens, this work focuses on the changes in the surface chemistry as a consequence of LSM. Furthermore, an AZ31 Mg alloy was used with the aim of avoiding the well-known galvanic effect of the second phases that form with high volume fraction for increasing concentrations of Al (primarily $Mg_{17}Al_{12}$), and act as local cathodic sites during corrosion. Surface analysis and electrochemical methods were used to evaluate the efficiency and suitability of LSM treatments for improving the corrosion resistance of Mg alloys.

2. Materials and methods

Commercially available AZ31 Mg alloy of composition 3.1 wt.% Al, 0.73 wt.% Zn, 0.25 wt.% Mn (balance Mg) supplied by Magnesium Elektron Ltd. was used as test spec-

imen. Plates of 20 × 20 × 5 mm were cut and successively ground using SiC emery paper to a 2000 grit finish under ethanol and polished to a 1 μm mirror finish before laser treatment. The test solution was 0.1 M NaCl (pH∼6) prepared from laboratory grade reagents and high purity water of 18.2MΩcm resistivity (Millipore^{TM} system).

A pulsed Nd:YAG laser (LOTIS LS 2147) with a frequency of 10 Hz and with Q-Switch mode was used. The pulse duration was 12–18 ns, operating in the fundamental mode of 1064 nm. The beam, with an average output energy up to 830 mJ (45 J pumping energy), was directed by a mirror to a convex bending lens with 150 mm focal length. The beam impinges the sample that was located inside a reaction chamber. The chamber was on an XY table controlled by a specific in-house developed software. The treatment was carried out in a protective argon atmosphere. The scanning speed was 1 mm/s and the overlapping of 250 μm with respect to the width of the bead. The laser fluence was of 14 and 17 J cm^{-2}. Lower and higher energy densities (10 and 20 J cm^{-2}) were also tested. However, these conditions were finally discarded. For 10 J cm^{-2}, the surface was not homogeneously melted, leaving parts of the specimen untreated; whereas 20 J cm^{-2} was determined to go beyond the damage threshold, often producing deep holes on the surface that protruded into the metallic matrix. For comparative purposes, a mirror finish polished non-LSM treated AZ31 specimen was also tested.

EIS measurements were performed potentiostatically in 0.1 M NaCl solution at the open circuit potential (OCP). A sinusoidal AC wave of ±10 mV (rms) amplitude was applied from 100 kHz to 0.1 Hz collecting 7 points per decade. Fitting of the EIS spectra was carried in out using the ZView® software (Scribner Associates). Potentiodynamic polarization (PDP) measurements were performed polarizing the test specimens in the anodic direction starting at the OCP to +700 mV vs. OCP at a scan rate of 1 mV/s.

All electrochemical measurements used a three-electrode configuration electrochemical cell, where the test specimen was the working electrode, a Ag/AgCl (3 M KCl) electrode (SSC) was the reference electrode and a platinum wire acted as the counter electrode. With the aim of maximizing the utility of the LSM treated surfaces for electrochemical testing, the syringe cell method developed by Panindre et al. [30] was used. This method allows for conventional electrochemical testing on small surface areas. Furthermore, the method has proved to be extremely suitable for assessment of localized corrosion susceptibility and is easy to set up. Details are available elsewhere [30]. In the present investigation, a standard 20 mL syringe with an inner diameter of the syringe mouth (tip of the barrel) of 1 mm was employed. This resulted in an exposed area of about 3.14 mm^2. All experiments were replicated several times as will be commented along with the corresponding reported results for clarity.

Table 1.

All electrochemical tests were carried out using a Gamry Instruments Interface 1000E potentiostat/galvanostat controlled by the Gamry Framework. Prior to polarization, all specimens were left at the OCP and the potential monitored until a stable value was observed.

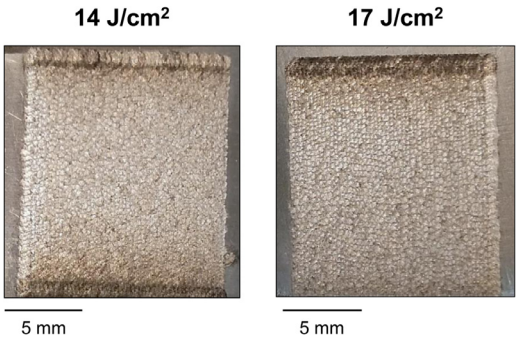

Fig. 1. Surface appearance of the AZ31 Mg alloy after LSM treatment at 14 and 17 J cm^{-2}.

Microstructural characterization of LSM treated AZ31 Mg alloys was performed using optical microscopy (OM). A Hitachi S 4800 scanning electron microscope (SEM) equipped with an Oxford Instruments energy dispersive X-ray (EDX) microanalyzer was used for surface and elemental analysis of the specimens after treatment. XPS measurements were carried out using a VG Microtech model MT 500 spectrometer equipped with a non-monochromatic $MgK_{\alpha 1.2}$ anode X-ray source operating at 300 W. A pressure below 10^{-9} torr was maintained during data collection. Adventitious C was used as binding energy (BE) reference, with 285.0 eV for C 1 s.

Surface profile roughness (Ra) was measured using a TR-200 stylus instrument by Innovatetst Europe with a cut-off length of 0.8 mm and total measurement length of 4 mm.

3. Results and discussion

3.1. Surface and chemical characterization after LSM treatment

Fig. 1 shows the surface appearance of the AZ31 Mg alloy after the LSM treatment at energy density values of 14 and 17 J cm^{-2}. Even though the non-treated specimen presented some submicrometer pits from the polishing (not shown), a smooth surface without corrosion products was observed. On the contrary, the LSM treated samples at 14 and 17 J cm^{-2} showed roughened surfaces. Fig. 2 shows the optical micrographs of the AZ31 Mg alloy after the LSM treatment at energy density values of 14 and 17 J cm^{-2}. It is evident from the micrographs in Fig. 2 that the laser impacts can be seen on the surface. This is due to the non-homogeneous energy distribution of the laser beam which is not a TEM00. Laser treated zones with maximum energy produces melting and rapid cooling and the impact spots of the laser were easily located, particularly at the lowest energy applied. The average value of Ra was determined from an average of 5 measurements with a deviation between the different measurements lower than 5%. While Ra for the untreated sample was 0.25 μm, Ra for the LSM treated samples was about 0.62 μm.

Table 1
Chemical surface composition expressed in atomic percentage (at.%) observed by XPS on the AZ31 Mg alloy without LSM treatment [24] and after the LSM treatment at energy density values of 14 and 17 J cm^{-2}.

Material	Chemical surface composition (at.%)						
	C	O	Mg	Al	O/(Mg+Al)	Mg/(Mg+Al) x100	Al/(Mg+Al) x100
No LSM	51	35	12	2	2.5	86	14
14 J cm^{-2}	34	48	14	4	3	77	23
17 J cm^{-2}	34	44	16	6	2	75	25

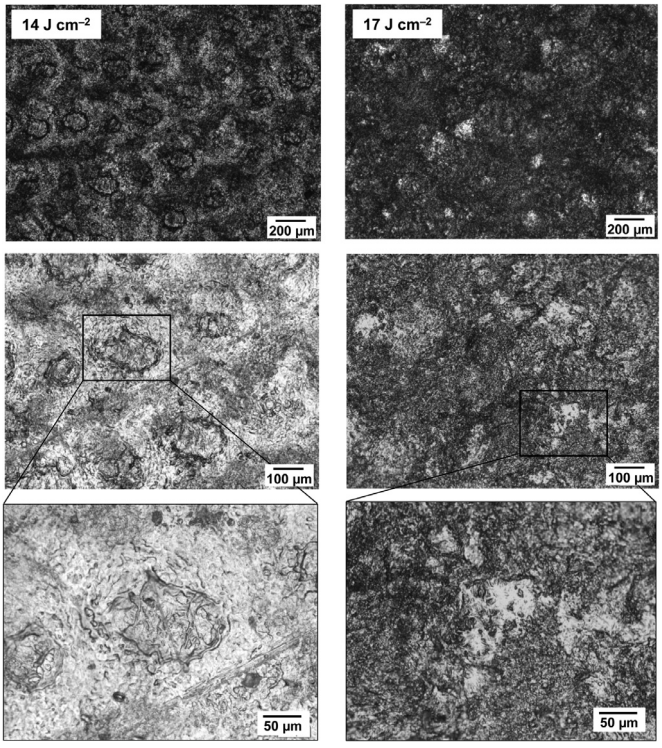

Fig. 2. Optical micrographs at different magnifications of the AZ31 Mg alloy after LSM treatment at 14 and 17 J cm^{-2}.

Chemical surface composition of the LSM treated samples at 14 and 17 J cm^{-2} was analyzed by X-ray photoelectron spectroscopy (XPS). As an example of the fitting, Fig. 3 shows the high resolution XPS spectra for O 1 s (Fig. 3a), Mg 2p (Fig. 3b) and Al 2p (Fig. 3c) of the LSM treated specimen at 14 J cm^{-2}. Spectrum for O 1 s shows only one peak associated with the presence of oxide species at binding energies of 531.4 eV. Spectra corresponding to Mg 2p (50.4 eV) and Al 2p (73.5 eV), also show one peak assigned to oxidized species of Mg^{2+} and Al^{3+}, respectively. It is interesting to note that no metallic components were observed for any of the LSM treated AZ31 surfaces. This indicates that the laser treatment generated a surface layer composed mainly of oxides of Mg and Al. Neither Zn nor Mn were detected in the surface oxide film.

Table 1 summarizes the concentration of the elements determined by XPS on the LSM treated samples at 14 and 17 J cm^{-2}, expressed in atomic percentages (at.%). For comparative purposes, Table 1 also includes the elemental composition of the AZ31 Mg alloy in polished condition as determined by our group in a previous study [31]. It is observed that the non LSM treated specimen presented a high content of C, which may be attributed to environmental contamination due to air and the ethanol used during polishing for surface preparation. On the contrary, the concentration of C on both the LSM treated specimens decreased significantly, likely due to the laser treatment. In the case of O, even though surface laser treatment was performed in the presence of Ar to minimize oxidation, greater concentrations of O were measured.

Given that the surface film was mainly composed of oxidized species of Mg and Al, the relative contribution of each element on the LSM specimens was analyzed by their corresponding cationic fraction (shown in Table 1). As an example, the cationic fraction for Al was calculated as follows: $Al_{cat} = Al^{3+} / (Mg^{2+} + Al^{3+})$. It can be observed that the surface cationic fraction of Al increased remarkably after the AZ31 Mg alloy was subjected to LSM treatment with respect to the polished specimen. This, as will be shown later, resulted in significant increased corrosion resistance in NaCl solution. Even though the cationic fraction of Al determined for both LSM treated specimens were similar, those corresponding to the surface treated at 17 J cm^{-2} exhibited slightly greater values. This is consistent with the notion that during laser treatment partial evaporation of Mg occurred, reducing its surface concentration and resulting in an enrichment of Al oxidized species.

Finally, it is reasonable that the laser treatment resulted in a non-uniform chemical composition in the surface oxide layer. Please note that energy density transmitted to the specimen during laser treatment is not homogeneous within the impact spot (unpublished work). In brief, maximum energy is reached at the beam center whereas decreased energies are found moving radially from the center towards the perimeter of the beam. Consequently, temperature gradients exist in the irradiated region, probably leading to non-homogeneous evaporation of Mg. Temperature gradients due to non-homogeneous energy densities within the irradiated spots also explain the roughened surfaces shown in Figs. 1 and 2.

3.2. Electrochemical impedance spectroscopy (EIS) measurements

Fig. 4 shows the Nyquist and Bode plots of the AZ31 Mg alloy without LSM treatment in 0.1 M NaCl solution. Results from a total of five replicates under the same experimental conditions are presented. A very good reproducibility was ob-

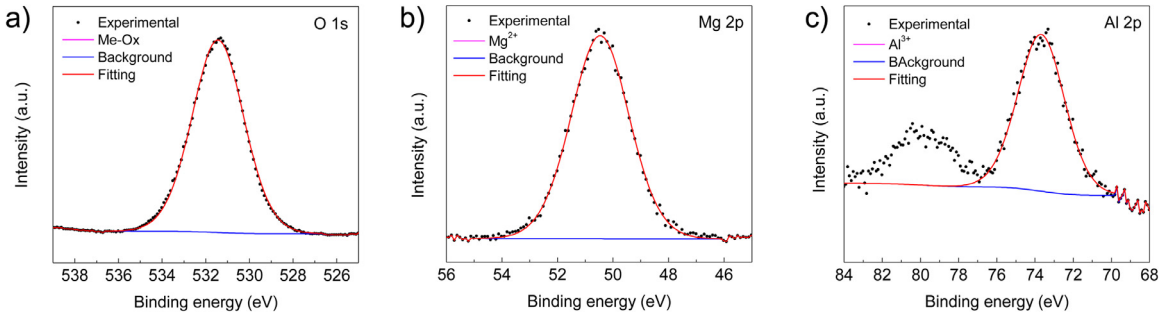

Fig. 3. High resolution XPS spectra for O 1 s, Mg 2p and Al 2p corresponding to the AZ31 Mg alloy after LSM treatment at 14 J cm^{-2}.

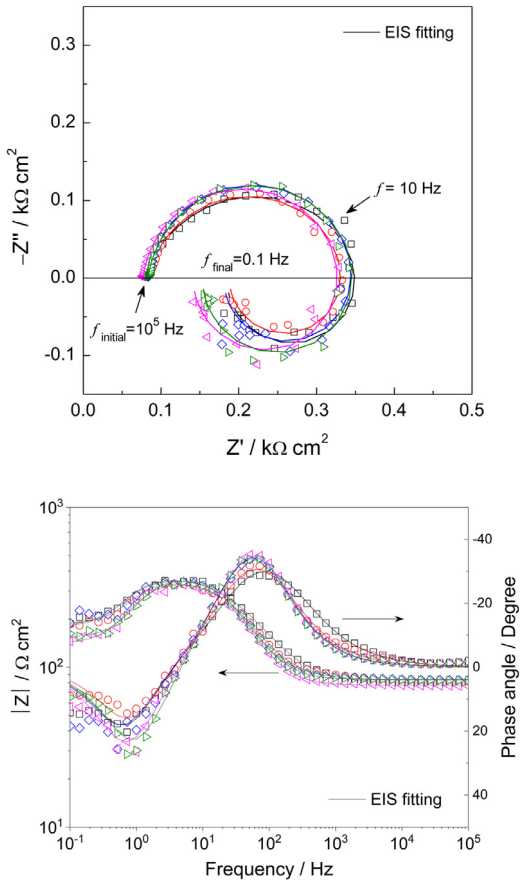

Fig. 4. Nyquist and Bode plots for the AZ31 Mg alloy without surface laser treatment in 0.1 M NaCl solution at room temperature. All curves correspond to independent replicates using the same experimental conditions measured at different regions of the surface.

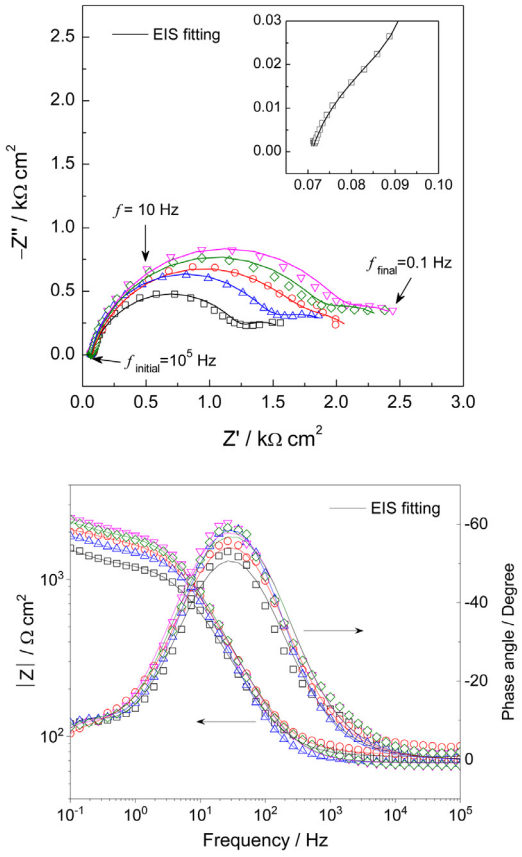

Fig. 5. Nyquist and Bode plots for the AZ31 Mg alloy after surface laser treatment at 14 J cm^{-2} in 0.1 M NaCl solution at room temperature. All curves correspond to independent replicates using the same experimental conditions measured at different regions of the surface.

tained, confirming the suitability of the syringe cell method for the electrochemical testing of Mg alloys. The presence of a capacitive and an inductive arc is observed in the Nyquist plot. The capacitive arc is represented in Fig. 4 by a negative component of the imaginary part (Z'') and the increase of the real component (Z') with the decrease in frequency to intermediate values. On the contrary, the inductive arc is represented by a positive component of Z'' and the decrease of Z' with the decrease of the frequency as it approaches to zero. This inductive behavior has been described previously in numerous independent studies in which the impedance response of Mg and its alloys was investigated [32–34].

Figs. 5 and 6 show the Nyquist and Bode plots of the AZ31 Mg alloy after the LSM treatment at energy density values of 14 and 17 J cm^{-2} in 0.1 M NaCl solution. As in the case of the AZ31 Mg alloy in the absence of LSM treatment, results from 5 replicated tests at each energy density carried out under identical experimental conditions are presented. It is evident that a wide dispersion of the results was obtained for both LSM treatment energies. Given that an excellent reproducibility was observed for the polished

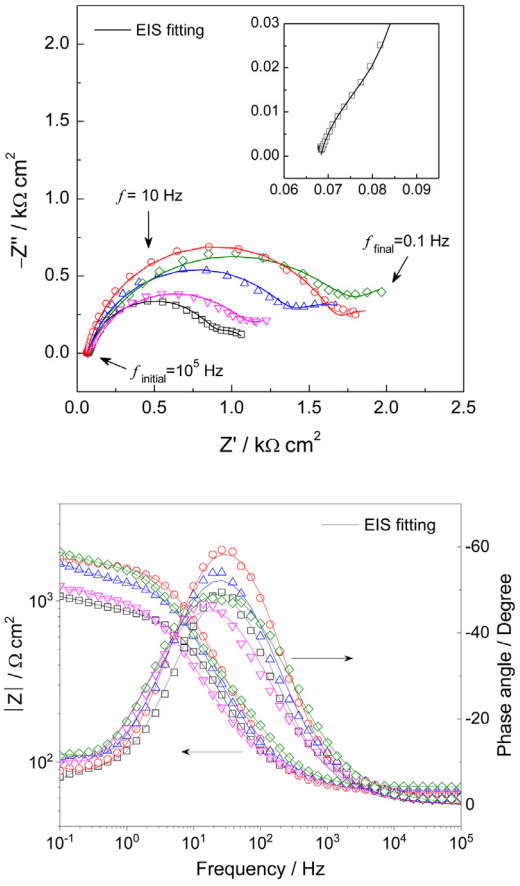

Fig. 6. Nyquist and Bode plots for the AZ31 Mg alloy after surface laser treatment at 17 J cm^{-2} in 0.1 M NaCl solution at room temperature. All curves correspond to independent replicates using the same experimental conditions measured at different regions of the surface.

AZ31 Mg alloy (see Fig. 4), the most reasonable explanation is that dispersion of the data was due to the high heterogeneity shown by the LSM treated surfaces (Figs. 1 and 2). These may be associated with local compositional changes due to non-homogeneous energy distribution during laser application. However, it is also likely that the differences in the EIS plots at each LSM energy density applied originated due to topographical variations. For instance, small variations of the surface area exposed to the electrolyte would result in capacitive arcs of varying diameter. Accurate determination of the exact area exposed during testing is not trivial. Due to this experimental limitation, all curves shown in Figs. 4-6 were normalized by the nominal area exposed to the electrolyte, defined by inner diameter of the syringe mouth. It should be mentioned that the curves shown in Figs. 5 and 6 correspond to 5 representative measurements of a higher number of tests performed on these surfaces where, in any case, curves with capacitive semicircle diameters above or below the limiting curves shown in Figs. 5 and 6 were obtained. Consequently, it is reasonable to assume that the global response of the LSM treated surfaces will be within the limits of these curves, and that the mean values of the electric elements that describe the impedance spectra (with their respective standard deviations) obtained from the fitting provide a reliable measure of the electrochemical behavior of the studied AZ31 Mg alloys LSM treated surfaces.

Prior to the analysis of the main features of the Nyquist plots presented in Figs. 4-6, the consistency of the experimental data was evaluated using the Kramers-Kronig (K-K) transforms [35,36]:

$$Z'(\omega) = Z'(\infty) + \frac{2}{\pi}\int_0^\infty \frac{xZ''(x) - \omega Z''(\omega)}{x^2 - \omega^2} dx \quad (1)$$

$$Z'(\omega) = Z'(0) + \frac{2}{\pi}\int_0^\infty \frac{(\omega/x)Z''(x) - Z''(\omega)}{x^2 - \omega^2} dx \quad (2)$$

$$Z''(\omega) = -\frac{2\omega}{\pi}\int_0^\infty \frac{Z'(x) - Z'(\omega)}{x^2 - \omega^2} dx \quad (3)$$

where Z'(x) and Z''(x) are the real and imaginary parts of the impedance, respectively, as a function of angular frequency (x), with $0 < x < \infty$; Z'(ω) and Z''(ω) are the real and imaginary parts of the impedance, respectively, for the angular frequency $x = \omega$. The KK transforms provide a measure of the robustness of the experimental results. In summary, using the K-K transforms it is possible to calculate the imaginary part of the impedance from the values of the real part obtained experimentally and compare them with the values of the imaginary part obtained experimentally. Alternatively, it is possible to calculate the values of the real part from the experimental values of the imaginary part. Fig. 7 shows the comparison between the experimental data and those calculated using the K-K transforms for one of each LSM treatment presented in Figs. 4-6 (i.e. no LSM treatment and LSM treatment at 14 and 17 J cm^{-2}). An excellent correlation between the experimental and the KK-transformed data was obtained. Even though only one plot is shown per condition for simplicity, all the curves presented in Figs. 4-6 exhibited a very good consistency between the experimental and the transformed data. Additionally, a statistical error function was used to compare the data obtained using the K-K transforms and the experimental data [37]. The errors calculated for all replicated tests were lower than 2.2% for the AZ31 Mg alloy without LSM treatment and 0.7 and 1.3% for the AZ31 Mg alloy subjected to LSM treatment at energy densities of 14 and 17 J cm^{-2}, respectively. The low calculated errors (less than 3%), and the good correlation shown in Fig. 7, confirm the validity of the experimental data.

Fig. 8 shows the equivalent electrical circuits (EEC) used to analyze the experimental EIS data of the AZ31 Mg alloy in the absence of LSM treatment (Fig. 8a) and the LSM treated AZ31 Mg alloys at energy density values of 14 and 17 J cm^{-2} (Fig. 8b) in 0.1 M NaCl solution. The EEC in Fig. 8a consists of a resistor (R_s) that simulates the resistance of the electrolyte between the working electrode (the Mg alloy) and the reference electrode, associated in series with the parallel combination of a constant phase element (CPE) and a resistor (R1), and the series association of an inductance

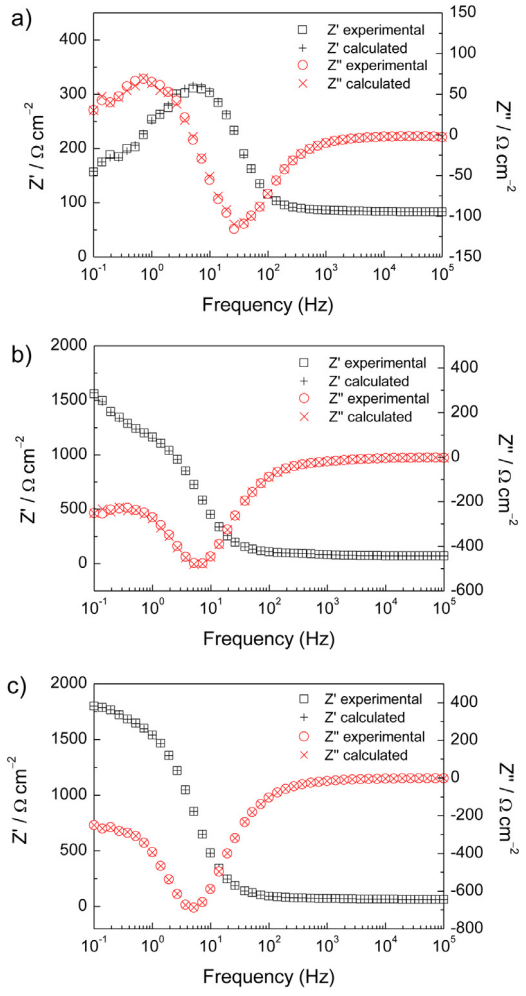

Fig. 7. Comparison of typical experimental impedance data for the AZ31 Mg alloy (a) without laser treatment, (b) after laser treatment at 14 J cm^{-2}, and (c) after laser treatment at 17 J cm^{-2}, from Figs. 4-6 and the impedance calculated using the Kramers-Kronig (KK) transforms.

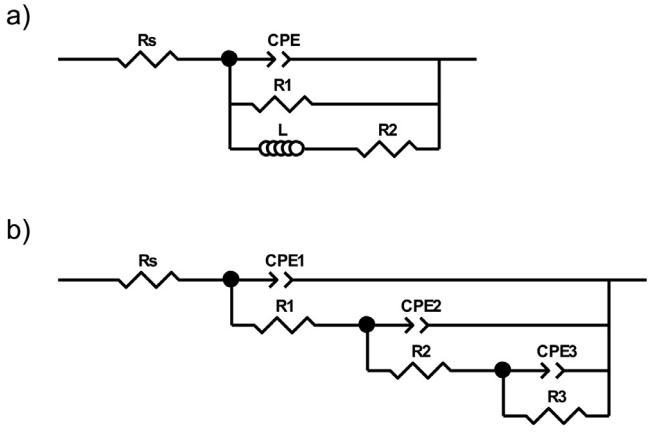

Fig. 8. Equivalent electrical circuits (EEC) used to fit the EIS spectra of the AZ31 Mg alloy (a) without LSM treatment, (b) after LSM treatment at 14 J cm^{-2} and 17 J cm^{-2} in 0.1 M NaCl.

(L) and a resistance (R2) [29,38]. A CPE was used instead of a capacitor to adequately simulate the capacitive response of the system. The CPE is an empirical admittance function that is usually used when the system cannot be described by an ideal capacitor, primarily due to the heterogeneous nature of the surface. The impedance of a CPE is defined by the following expression:

$$Z_{CPE} = \frac{1}{Y(j\omega)^n} \tag{4}$$

where Y is the value of the admittance (S cm^{-2} s^n), ω is the angular frequency (rad s^{-1}), j is the imaginary number ($j^2 = (-1)$) and n is a dimensionless fractional exponent that takes values between –1 and 1. When $n = 1$, the CPE represents an ideal capacitor; when $n = 0$, the CPE represents a resistance; and when $n = -1$, the CPE represents an inductor. In the EEC of Fig. 8a, the CPE is associated with the capacitance of the electrochemical double layer and R1 is the charge transfer resistance (R_{ct}). The series combination of L and R2 was used to simulate the inductive response of the system, and is normally associated with the presence of reaction intermediates or adsorbed species on the electrode surface during the corrosion reaction. A detailed explanation of the physical meaning of the electrical elements that simulate the inductive response in the EEC of Fig. 8a is not trivial and is currently the subject of debate. Recently, Yuwono et al. [39] studied the dissolution mechanism of Mg and the concomitant anomalous hydrogen evolution using first-principles density functional theory calculations and proposed the existence of intermediate species adsorbed on the metal surface that would be involved in these phenomena. It is possible that the presence of the inductive behavior observed in this investigation and in a large number of independent works on the corrosion of Mg is related to the presence of those intermediates.

With respect to the AZ31 Mg alloys after LSM treatment at energy density values of 14 and 17 J cm^{-2}, the Nyquist plots in Figs. 5 and 6 show three different capacitive arcs (i.e. at high, medium and low frequencies). Consequently, a three-time constant EEC (Fig. 8b) was used to model the electrochemical response of the specimens during testing. The EEC in Fig. 8b shows a multi-component nested Randle's circuits where the minimum number of capacitive time-constants to reliably represent the data was used [33,34]. The physical meaning of each of the electrical elements used will be briefly discussed later. Interestingly, no inductive behavior was observed for any of the LSM treated Mg alloys in the same frequency range where the specimens in the absence of LSM treatment exhibited a clear inductive response. For this reason, no series association of an inductance and a resistance were included in the EEC. This is likely due to a greater corrosion resistance associated with the formation of a protective surface film that hindered dissolution. All curves in Figs. 4-6 show an excellent correlation between the experimental and the fitted data.

Tables 2-4 show the results obtained from the fitting of the Nyquist plots in Figs. 4-6 using the EECs shown in

Table 2
Fitting results of EIS experimental data for the polished AZ31 Mg alloy without LSM treatment in 0.1 M NaCl solution. Data from 5 replicated measurements are presented.

Test	R_s (Ω cm^2)	Y (μS cm^{-2} s^{n1})	n_1	R_1 (Ω cm^2)	L (Ω s cm^2)	R_2 (Ω cm^2)	χ^2
1	79	47	0.81	287	76	166	9×10^{-3}
2	83	43	0.87	260	65	175	9×10^{-3}
3	84	31	0.93	268	77	151	3×10^{-2}
4	77	34	0.93	257	49	86	8×10^{-3}
5	83	37	0.91	275	41	94	7×10^{-3}

Table 3
Fitting results of EIS experimental data for the LSM treated AZ31 Mg alloy at an energy density of 14 J cm^{-2} in 0.1 M NaCl solution. Data from 5 replicated measurements are presented.

Test	R_s (Ω cm^2)	Y_1 (μS cm^{-2} s^{n1})	n_1	R_1 (Ω cm^2)	Y_2 (μS cm^{-2} s^{n2})	n_2	R_2 (Ω cm^2)	Y_3 (mS cm^{-2} s^{n3})	n_3	R_3 (Ω cm^2)	χ^2
1	71	26	0.83	65	10	0.98	1106	2.18	0.90	456	2×10^{-4}
2	71	11	0.80	19	21	0.89	1611	1.48	0.67	631	3×10^{-4}
3	66	13	0.90	12	14	0.93	1418	1.77	0.77	704	2×10^{-4}
4	65	16	0.86	81	93	0.96	1869	1.46	0.87	645	3×10^{-4}
5	65	20	0.85	95	65	0.99	1737	1.42	0.92	605	4×10^{-4}

Table 4
Fitting results of EIS experimental data for the LSM treated AZ31 Mg alloy at an energy density of 17 J cm^{-2} in 0.1 M NaCl solution. Data from 5 replicated measurements are presented.

Test	R_s (Ω cm^2)	Y_1 (μS cm^{-2} s^{n1})	n_1	R_1 (Ω cm^2)	Y_2 (μS cm^{-2} s^{n2})	n_2	R_2 (Ω cm^2)	Y_3 (mS cm^{-2} s^{n3})	n_3	R_3 (Ω cm^2)	χ^2
1	68	29	0.86	50	16	0.95	752	2.97	0.76	289	2×10^{-4}
2	68	24	0.87	68	15	0.91	1 233	2.12	0.81	665	3×10^{-4}
3	77	34	0.83	60	25	0.91	1 101	2.77	0.84	876	2×10^{-4}
4	68	51	0.81	87	33	0.86	953	4.96	0.89	335	3×10^{-4}
5	64	17	0.88	24	12	0.92	1 602	3.74	0.90	499	4×10^{-4}

Fig. 8. Each Table shows the fitting results of the 5 measurements presented in Figs. 4-6. While the CPE parameters (Y and n) provide information on the capacitive behavior of the system, the combination of resistances is associated with the polarization resistance (R_p). In brief, the Stern-Geary equation predicts that for a metal under activation control R_p is inversely related to the corrosion current density (i_{corr}) by the proportionality constant B, which depends exclusively on the Tafel slopes [40]. King et al. [33] demonstrated the importance of accounting for the inductive behavior of dissolving Mg for the accurate determination of R_p and, in consequence, of i_{corr}. Assuming that the B constant does not change dramatically with the LSM treatment, it is possible to evaluate the corrosion resistance of the AZ31 Mg alloys without LSM treatment and LSM treated at energy densities of 14 and 17 J cm^{-2} by simply comparing their respective R_p values obtained from the EIS fitting.

Tables 5 and 6 summarize the fitting results presented in Tables 2-4 showing the mean values and their corresponding standard deviation for each of the elements in the EEC shown in Fig. 8. Please note that in Tables 5 and 6 no CPE admittance values (Y) are presented. Instead, effective capacitances (C_{eff}) are provided. The admittance of a CPE is not expressed in units of capacitance and, as shown in Eq. (4), is dependent of an exponent. Small deviations of that exponent with respect to 1 (ideal capacitor) can result in large errors if Y is used as a capacitance. However, it is possible to convert Y into C_{eff} using the expression developed by Brug et al. [41]:

Table 5
Fitting results of EIS experimental data for the AZ31 Mg alloy without LSM treatment in 0.1 M NaCl solution. Mean values and their corresponding standard deviation for each of the elements in the EEC shown in Fig. 8a are presented. CPE elements expressed as C_{eff} calculated using Eq. (5).

		No Laser
R_s	(Ω cm^2)	81 ± 3
$C_{eff,1}$	(μF cm^{-2})	18 ± 3
R_1	(Ω cm^2)	270 ± 12
R_2	(Ω cm^2)	134 ± 42
L	(Ω s cm^2)	62 ± 16

$$C_{eff} = Y^{\frac{1}{n}}\left(R_s^{-1} + R_F^{-1}\right)^{\frac{n-1}{n}} \quad (5)$$

where R_F is the faradaic resistance in parallel with the capacitance to be determined and the rest of the terms have already been defined.

It can be seen that for the AZ31 Mg alloy without LSM treatment, $C_{eff,1}$ is of the order of 20 μF cm^{-2}, which corresponds to typical values for the capacitance of an electrochemical double layer. The fact that the CPE1 in Fig. 8 is associated with the capacity of the double layer confirms that R1 is associated with the charge transfer resistance (R_{ct}). In the case of the LSM treated AZ31 Mg alloys, $C_{eff,1}$ and $C_{eff,2}$ presented similar values of the order of 10 μF cm^{-2},

Table 6
Fitting results of EIS experimental data for the AZ31 Mg alloy after LSM treatment at energy densities of 14 and 17 J cm^{-2} in 0.1 M NaCl solution. Mean values and their corresponding standard deviation for each of the elements in the EEC shown in Fig. 8b are presented. CPE elements expressed as C_{eff} calculated using Eq. (5).

		14 J cm^{-2}	17 J cm^{-2}
R_s	(Ω cm^2)	67 ± 3	69 ± 5
$C_{eff,1}$	(μF cm^{-2})	5 ± 2	9 ± 2
R_1	(Ω cm^2)	54 ± 37	58 ± 23
$C_{eff,2}$	(μF cm^{-2})	8 ± 1	10 ± 3
R_2	(Ω cm^2)	1548 ± 298	1128 ± 319
$C_{eff,3}$	(μF cm^{-2})	1054 ± 468	2480 ± 1196
R_3	(Ω cm^2)	608 ± 93	533 ± 242

complicating their assignation to a certain relaxation process. Nevertheless, the slightly lower values of $C_{eff,1}$ are consistent with the capacitance of an oxide film, which is in agreement with the XPS surface analysis. On the other hand, even though $C_{eff,2}$ values are moderately small for an electric double layer, they may be associated with the double layer capacitance. Finally, the time constant at the lowest frequencies ($C_{eff,3}$) presents values of approximately 2200 and 5300 μF cm^{-2} for energies densities of 14 and 17 J cm^{-2}, respectively. The physical meaning of these pseudo-capacitances is not evident. They may be associated with finite diffusional processes [42,43]. However, it is possible that these pseudo-capacitances were due to adsorption accompanied by charge transfer [42]. This notion is in agreement with the mechanism proposed by Yuwono et al. [39].

Regarding the R_p values, they can be estimated from the resistances in Tables 5 and 6 by simplifying the system for the case in which the frequency tends to zero (f → 0):

$$\frac{1}{R_p} = \frac{1}{R_1} + \frac{1}{R_2} \tag{6}$$

$$\frac{1}{R_p} = \frac{1}{R_1 + R_2 + R_3} \tag{7}$$

where Eqns. (6) and (7) correspond to the case of the AZ31 Mg alloy without LSM treatment and the LSM treated AZ31 Mg alloys, respectively.

Fig. 9 shows the calculated R_p values for the AZ Mg alloy without LSM treatment and LSM treated at 14 and 17 J cm^{-2} in 0.1 M NaCl solution determined from the EIS spectra shown in Figs. 4-6. The LSM treatment increased remarkably the values of R_p for the AZ31 Mg alloy with respect to the non-treated surface, indicating lower corrosion rates. Furthermore, the LSM treatment at 14 J cm^{-2} provided a slightly greater R_p values than that at 17 J cm^{-2}.

3.3. Potentiodynamic anodic polarization measurements

The anodic kinetics was studied by means of potentiodynamic polarization. Fig. 10 shows the potentiodynamic anodic polarization curves of the AZ31 Mg alloy without LSM treatment and after the LSM treatment at energy density values of 14 and 17 J cm^{-2} in 0.1 M NaCl solution. For simplicity,

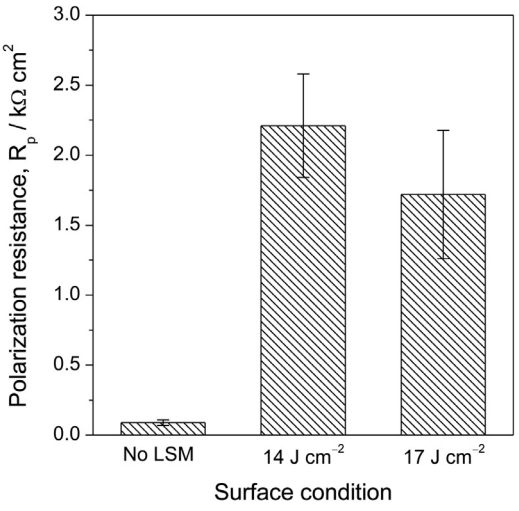

Fig. 9. Polarization resistance values obtained by EIS for the AZ31 Mg alloy without LSM treatment, and after LSM treatment at 14 J cm^{-2} and 17 J cm^{-2} in 0.1 M NaCl solution. Mean values from replicated experiments are presented. Error bars are standard deviation.

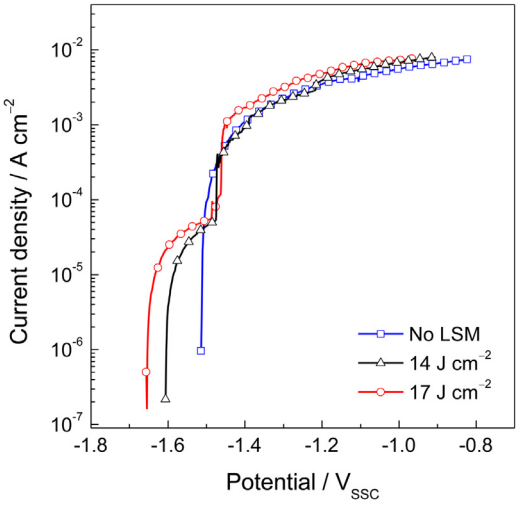

Fig. 10. Potentiodynamic polarization curves of the AZ31 Mg alloy without LSM treatment, and after LSM treatment at 14 J cm^{-2} and 17 J cm^{-2} in 0.1 M NaCl solution. The scan rate was 1 mV/s. Typical results from replicated experiments are presented.

one typical curve from replicated tests is presented for each condition. Significant differences were observed between the three specimens. The AZ31 Mg alloy without LSM treatment showed an E_{corr} of about −1.5 V_{SSC} and no sign of passivity with increasing current densities at potentials above the E_{corr}. This behavior, typical of an ideally non-polarizable electrode, has been previously observed for the AZ31 Mg alloy in many independent works [14,44-46]. On the contrary, the AZ31 Mg alloy specimens previously subjected to LSM treatment exhibited more negative E_{corr} values and clear passive-like regions of around 100 mV followed by a sharp increase of the current density, which is indicative of localized corrosion. These results are in agreement with the increased R_p values estimated using EIS (see Fig. 9) and support the notion that LSM treat-

ment enhances the corrosion resistance of AZ31 Mg alloy in a chloride containing solution. Furthermore, differences were observed between the LSM treated AZ31 Mg alloys at energy density values of 14 and 17 J cm^{-2}. While the specimen treated at 14 J cm^{-2} presented an E_{corr} of about −1.60 V_{SSC}, the AZ31 treated at 17 J cm^{-2} exhibited a lower E_{corr} value of approximately −1.65 V_{SSC}. Another interesting difference between the two LSM energy densities applied was observed in the passive regions, where the specimen treated at the lower energy showed the lowest current densities thus the more protective surface against corrosion. Even though the cathodic kinetics was not investigated, it is clear that the LSM treatment decreased rate of HE. It is reasonable that this decreased cathodic kinetics was responsible for the lower values of E_{corr} and the ability to observe the passive behavior in a potential region that was dominated by the cathodic reaction for the AZ31 Mg alloy without LSM treatment.

In summary, the potentiodynamic anodic polarization results confirm the EIS observations where the LSM treatment on the AZ31 Mg alloy resulted in enhanced corrosion resistance. Furthermore, the lower current densities measured in the passive regions for the AZ31 Mg alloy treated at 14 J cm^{-2} are in agreement with the EIS determined R_p values, where the AZ31 Mg treated at this energy density were the greatest.

Fig. 11 shows the optical micrographs of the AZ31 Mg alloy specimens without LSM treatment, and after LSM treatment at 14 J cm^{-2} and 17 J cm^{-2} after anodic polarization in 0.1 M NaCl solution. All specimens exhibited the typical black corrosion products that are normally observed after Mg alloy corrosion. However, while the sample without prior LSM treatment showed circular-like attacked regions with the black corrosion product layer extending radially on the surface, a different morphology was observed for the AZ31 Mg alloy specimens that had been previously subjected to LSM treatment at 14 J cm^{-2} and 17 J cm^{-2}. In these cases, significantly less corroded surfaces were exhibited, with a number of localized corroded regions distributed on the sample. This is consistent with the XPS results that revealed an enrichment of Al in the surface after LSM treatment at both energy densities. Furthermore, the localized attack observed in the surface appearance of the previously LSM treated samples (Fig. 11) is also in accordance with the passive regions found during potentiodynamic anodic polarization (Fig. 10).

Fig. 12 provides a closer look to the corroded regions on the surface of the AZ31 Mg alloy without LSM treatment. SEM micrographs show a dense and rather compact corrosion product layer with the presence of numerous cracks (Fig. 12a). Higher magnification SEM micrographs reveal that the corrosion product exhibited a crystalline microstructure. Elemental analysis obtained by EDS on a number of sites on the corroded areas showed that the corrosion product consisted mainly of Mg and O at a O/Mg ratio equal to 1.8 ± 0.2. This is very close to the expected value of 2 for $Mg(OH)_2$, suggesting that the corrosion product film was primarily composed of this species.

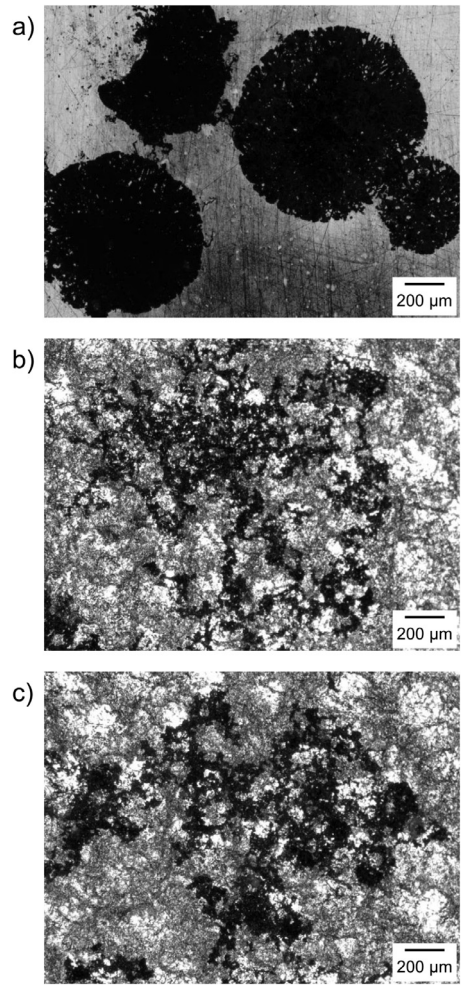

Fig. 11. Optical micrographs of the AZ31 Mg alloy without LSM treatment, and after LSM treatment at 14 J cm^{-2} and 17 J cm^{-2} after potentiodynamic anodic polarization in 0.1 M NaCl solution. .

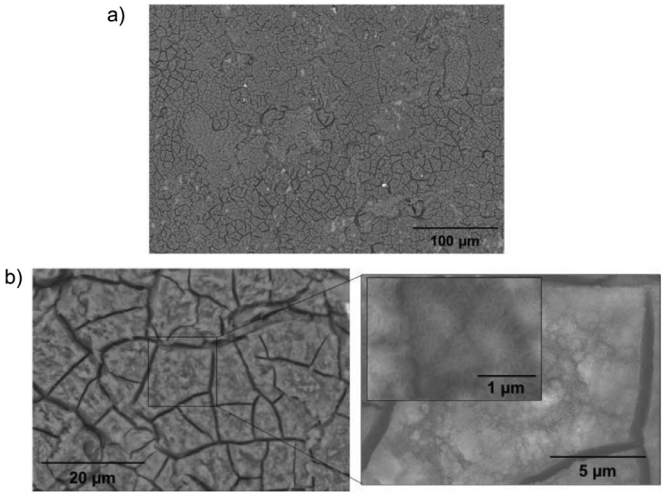

Fig. 12. BSE SEM micrographs of the corroded regions on the AZ31 Mg alloy without prior LSM after potentiodynamic anodic polarization in 0.1 M NaCl solution, shown in Fig. 11a.

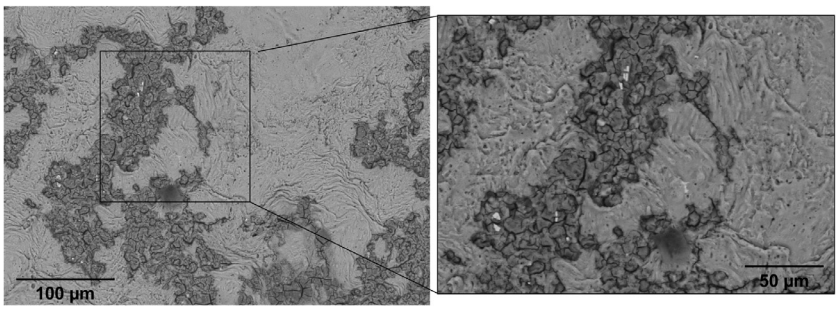

Fig. 13. BSE SEM micrographs of the corroded regions on the AZ31 Mg alloy subjected to LSM treatment at 14 J cm^{-2} after potentiodynamic anodic polarization in 0.1 M NaCl solution, shown in Fig. 11b.

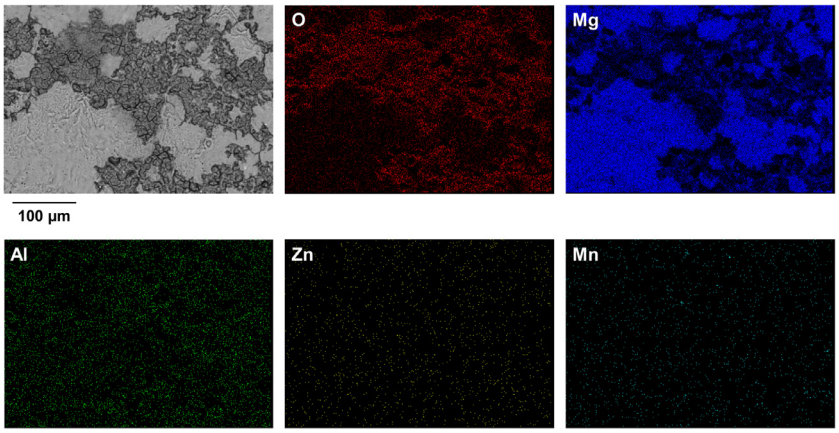

Fig. 14. EDX maps for elemental composition of the corroded regions on the AZ31 Mg alloy subjected to LSM treatment at 14 J cm^{-2} after potentiodynamic anodic polarization in 0.1 M NaCl solution.

Regarding the corroded regions on the AZ31 Mg alloy specimens previously subjected to LSM treatment, a nearly identical behavior was observed. For this reason, only the SEM micrographs corresponding to the corroded regions on the LSM sample treated at 14 J cm^{-2} are shown in Fig. 13. In contrast with the Mg alloy without LSM treatment, the fraction of the surface covered with corrosion products was significantly lower. This is consistent with a more corrosion resistant surface film and is in agreement with the results from the electrochemical tests. Despite the differences in the amount of corrosion products, morphology of the corroded regions was similar to that observed for the Mg alloy without LSM treatment. A dense and cracked corrosion product layer was clearly exhibited. Furthermore, Fig. 13 also shows the presence of a small amount of tiny and mostly elongated particles. EDS analysis (not shown here for brevity) confirmed that they consisted of Al, Mn and Fe, which is consistent with Al-Mn-Fe intermetallic second phases.

Element distribution of the corroded regions on the LSM sample treated at 14 J cm^{-2} was carried out by EDS elemental maps, shown in Fig. 14. As previously commented, this is representative of both energy densities used for LSM treatment. Compositional analysis showed that the corrosion product film exhibited a high concentration of oxygen. Interestingly, Mg concentration was lower in the corrosion products than in the non-corroded regions. Area analysis in randomly selected zones of the corroded and non-corroded regions revealed that Mg concentration was 41.0 ± 0.2 and 78 ± 1 at.%, respectively. This explains that, even though the corrosion product film mainly consisted in oxidized species of Mg, no significant contrast in the Mg signal was observed in the EDS maps. Furthermore, O/Mg ratio in the corroded regions was about 1.38 ± 0.01, indicating a lower contribution of $Mg(OH)_2$ to the corrosion product than for the non-LSM treated specimen and suggesting that it was composed of a mixture of MgO and $Mg(OH)_2$. Finally, the EDS elemental maps depicted in Fig. 14 show that the other detected elements were homogenously distributed over the scanned area with no appreciable enrichment in the corrosion product film.

4. Conclusions

The effect of LSM treatment on the corrosion resistance of AZ31 Mg alloy was investigated using surface characterization, electrochemical impedance spectroscopy and potentiodynamic polarization. Different laser processing conditions (energy densities of 14 and 17 J cm^{-2}) were used. The main conclusions are:

- LSM treatment induced topographical and compositional changes with respect to a polished AZ31 Mg alloy specimen. Rougher surfaces composed of a surface layer enriched in Al were observed.

- Electrochemical impedance showed that LSM treatment significantly increased R_p in the AZ31 Mg alloy, leading to decreased values of corrosion rate.
- LSM treatment at both energy densities hindered anodic dissolution. Potentiodynamic polarization revealed a small passive-like region of about 100 mV.
- No significant differences in the corrosion resistance of the LSM treated AZ31 Mg alloys were observed between the different energy densities used for LSM treatment.
- These findings are in agreement with the notion that localized heating of the surface due to laser irradiation yields to preferential evaporation of Mg, resulting in greater surface concentrations of more protective Al.
- For the immersion times used in this study, LSM treatment increased the corrosion resistance of AZ31 Mg alloy under open circuit conditions and anodic polarization.

Declaration of Competing Interest

The authors declare that they have no known competing financial interests or personal relationships that could have appeared to influence the work reported in this paper.

Acknowledgements

S. Fajardo expresses his gratitude to the State Research Agency (Ministry of Science and Innovation of Spain), the Spanish National Research Council (CSIC) and the European Regional Development Fund (ERDF) for the support under the project RYC2019–027006-I (AEI/FEDER/UE). The authors thank the CENIM Surface Characterization (XPS) and Electron Microscopy Laboratories.

References

[1] E. Aghion, B. Bronfin, D. Eliezer, The role of the magnesium industry in protecting the environment, J. Mater. Process. Technol. 117 (2001) 381–385, doi:10.1016/S0924-0136(01)00779-8.
[2] D. Kumar, R.K. Phanden, L. Thakur, A Review On Environment Friendly and Lightweight Magnesium-Based metal Matrix Composites and Alloys, Mater. Today, in press, 2020, doi:10.1016/j.matpr.2020.07.424.
[3] M. Esmaily, J.E. Svensson, S. Fajardo, N. Birbilis, G.S. Frankel, S. Virtanen, R. Arrabal, S. Thomas, L.G. Johansson, Fundamentals and advances in magnesium alloy corrosion, Prog. Mater. Sci. 89 (2017) 92–193, doi:10.1016/j.pmatsci.2017.04.011.
[4] S. Virtanen, Biodegradable Mg and Mg alloys: corrosion and biocompatibility, Mater. Sci. Eng. B 176 (2011) 1600–1608, doi:10.1002/maco.200303689.
[5] M. Alvarez-Lopez, M.D. Pereda, J.A. Del Valle, M. Fernandez-Lorenzo, M.C. Garcia-Alonso, O.A. Ruano, M.L. Escudero, Corrosion behaviour of AZ31 magnesium alloy with different grain sizes in simulated biological fluids, Acta Biomater 6 (2010) 1763–1771, doi:10.1016/j.actbio.2009.04.041.
[6] K.R. R, S. Bontha, M.R. R, M. Das, V.K. Balla, Laser surface melting of Mg-Zn-Dy alloy for better wettability and corrosion resistance for biodegradable implant applications, Appl. Surf. Sci. 480 (2019) 70–82, doi:10.1016/j.apsusc.2019.02.167.
[7] T.B. Abbott, Magnesium: industrial and Research Developments Over the Last 15 Years, Corrosion 71 (2015) 120–127, doi:10.5006/1474.
[8] A. Singh, S. Harimkar, Laser surface engineering of magnesium alloys: a review, JOM 64 (2012) 716–733, doi:10.1007/s11837-012-0340-2.
[9] V. Manakari, G. Parande, M. Gupta, Selective Laser Melting of Magnesium and Magnesium Alloy Powders: a Review, Metals (Basel) 7 (2016) 2, doi:10.3390/met7010002.
[10] A.E. Coy, F. Viejo, F.J. Garcia-Garcia, Z. Liu, P. Skeldon, G.E. Thompson, Effect of excimer laser surface melting on the microstructure and corrosion performance of the die cast AZ91D magnesium alloy, Corros. Sci. 52 (2010) 387–397, doi:10.1016/j.corsci.2009.09.025.
[11] C. Zeng, J. Shen, C. He, M. Zhou, An ultrathin melted layer on magnesium alloy manufactured by low power laser, Mater. Res. Express 6 (2019) 066527, doi:10.1088/2053-1591/ab0cbe.
[12] C. Liu, J. Liang, J. Zhou, L. Wang, Q. Li, Effect of laser surface melting on microstructure and corrosion characteristics of AM60B magnesium alloy, Appl. Surf. Sci. 343 (2015) 133–140, doi:10.1016/j.apsusc.2015.03.067.
[13] T.-.C. Wu, Y.-.H. Ho, S. Joshi, R. Rajamure, N. Dahotre, Microstructure and corrosion behavior of laser surface-treated AZ31B Mg bio-implant material, Lasers Med. Sci. 32 (2017) 1–7, doi:10.1007/s10103-017-2174-1.
[14] A.G. Rakoch, E.P. Monakhova, Z.V. Khabibullina, M. Serdechnova, C. Blawert, M.L. Zheludkevich, A.A. Gladkova, Plasma electrolytic oxidation of AZ31 and AZ91 magnesium alloys: comparison of coatings formation mechanism, J. Magnes. Alloy 8 (2020) 587–600, doi:10.1016/j.jma.2020.06.002.
[15] S. Yagi, A. Sengoku, K. Kubota, E. Matsubara, Surface modification of ACM522 magnesium alloy by plasma electrolytic oxidation in phosphate electrolyte, Corros. Sci. 57 (2012) 74–80, doi:10.1016/j.corsci.2011.12.032.
[16] L. Wang, J. Zhou, J. Liang, J. Chen, Microstructure and corrosion behavior of plasma electrolytic oxidation coated magnesium alloy pretreated by laser surface melting, Surf. Coat. Technol. 206 (2012) 3109–3115, doi:10.1016/j.surfcoat.2011.12.040.
[17] B. Gao, S. Hao, J. Zou, W. Wu, G. Tu, C. Dong, Effect of high current pulsed electron beam treatment on surface microstructure and wear and corrosion resistance of an AZ91HP magnesium alloy, Surf. Coat. Technol. 201 (2007) 6297–6303, doi:10.1016/j.surfcoat.2006.11.036.
[18] C. Taltavull, B. Torres, A.J. Lopez, P. Rodrigo, E. Otero, A. Atrens, J. Rams, Corrosion behaviour of laser surface melted magnesium alloy AZ91D, Mater. Des. 57 (2014) 40–50, doi:10.1016/j.matdes.2013.12.069.
[19] J. Dutta Majumdar, R. Galun, B.L. Mordike, I. Manna, Effect of laser surface melting on corrosion and wear resistance of a commercial magnesium alloy, Mater. Sci. Eng. A 361 (2003) 119–129, doi:10.1016/S0921-5093(03)00519-7.
[20] G. Abbas, Z. Liu, P. Skeldon, Corrosion behaviour of laser-melted magnesium alloys, Appl. Surf. Sci. 247 (1) (2005) 347–353.
[21] P.C. Banerjee, R.K.S. Raman, Y. Durandet, G. McAdam, Electrochemical investigation of the influence of laser surface melting on the microstructure and corrosion behaviour of ZE41 magnesium alloy – an EIS based study, Corros. Sci. 53 (2011) 1505–1514, doi:10.1016/j.corsci.2011.01.017.
[22] W. Khalfaoui, E. Valerio, J.E. Masse, M. Autric, Excimer laser treatment of ZE41 magnesium alloy for corrosion resistance and microhardness improvement, Opt. Laser Eng. 48 (2010) 926–931, doi:10.1016/j.optlaseng.2010.03.009.
[23] D. Dubé, M. Fiset, A. Couture, I. Nakatsugawa, Characterization and performance of laser melted AZ91D and AM60B, Mater. Sci. Eng. A 299 (2001) 38–45, doi:10.1016/S0921-5093(00)01414-3.
[24] Y. Yang, X. Xiong, J. Chen, X. Peng, D. Chen, F. Pan, Research advances in magnesium and magnesium alloys worldwide in 2020, J. Magnes. Alloy. 9 (2021) 705–747, doi:10.1016/j.jma.2021.04.001.
[25] F. Iranshahi, M.B. Nasiri, F.G. Warchomicka, C. Sommitsch, Corrosion behavior of electron beam processed AZ91 magnesium alloy, J. Magnes. Alloy. 8 (2020) 1314–1327, doi:10.1016/j.jma.2020.08.012.

[26] X. Zhang, K. Zhang, J. Zou, P. Yan, L. Song, Y. Liu, Surface microstructure modifications and in-vitro corrosion resistance improvement of a WE43 Mg alloy treated by pulsed electron beams, Vacuum 173 (2020) 109132, doi:10.1016/j.vacuum.2019.109132.

[27] Y.R. Liu, K.M. Zhang, J.X. Zou, D.K. Liu, T.C. Zhang, Effect of the high current pulsed electron beam treatment on the surface microstructure and corrosion resistance of a Mg-4Sm alloy, J. Alloy. Compd. 741 (2018) 65–75, doi:10.1016/j.jallcom.2017.12.227.

[28] W.J. Lee, J. Kim, H.W. Park, Improved corrosion resistance of Mg alloy AZ31B induced by selective evaporation of Mg using large pulsed electron beam irradiation, J. Mater. Sci. Technol. 35 (2019) 891–901, doi:10.1016/j.jmst.2018.12.004.

[29] M.C. Delgado, F.R. García-Galvan, I. Llorente, P. Pérez, P. Adeva, S. Feliu, Influence of aluminium enrichment in the near-surface region of commercial twin-roll cast AZ31 alloys on their corrosion behaviour, Corros. Sci. 123 (2017) 182–196, doi:10.1016/j.corsci.2017.04.027.

[30] A.M. Panindre, K.H. Chang, T. Weirich, G.S. Frankel, Technical note: syringe cell for electrochemical testing, Corrosion 74 (2018) 847–850, doi:10.5006/2847.

[31] S. Feliu Jr, C. Maffiotte, A. Samaniego, J.C. Galván, V. Barranco, Effect of the chemistry and structure of the native oxide surface film on the corrosion properties of commercial AZ31 and AZ61 alloys, Appl. Surf. Sci. 257 (2011) 8558–8568, doi:10.1016/j.apsusc.2011.05.014.

[32] V. Shkirskiy, A.D. King, O. Gharbi, P. Volovitch, J.R. Scully, K. Ogle, N. Birbilis, Revisiting the electrochemical impedance spectroscopy of magnesium with online inductively coupled plasma atomic emission spectroscopy, Chem. Phys. Chem. 16 (2015) 536–539, doi:10.1002/cphc.201402666.

[33] A.D. King, N. Birbilis, J.R. Scully, Accurate electrochemical measurement of magnesium corrosion rates; a combined impedance, mass-loss and hydrogen collection study, Electrochim. Acta 121 (2014) 394–406, doi:10.1016/j.electacta.2013.12.124.

[34] L.G. Bland, A.D. King, N. Birbilis, J.R. Scully, Assessing the Corrosion of Commercially Pure Magnesium and Commercial AZ31B by Electrochemical Impedance, Mass-Loss, Hydrogen Collection, and Inductively Coupled Plasma Optical Emission Spectrometry Solution Analysis, Corrosion 71 (2015) 128–145, doi:10.5006/1419.

[35] J.R. Macdonald, Some new directions in impedance spectroscopy data analysis, Electrochim. Acta 38 (1993) 1883–1890 https://doi.org/10.1016/0013-4686(93)80310-V.

[36] S. Fajardo, D.M. Bastidas, M. Criado, J.M. Bastidas, Electrochemical study on the corrosion behaviour of a new low-nickel stainless steel in carbonated alkaline solution in the presence of chlorides, Electrochim. Acta 129 (2014) 160–170, doi:10.1016/j.electacta.2014.02.107.

[37] J. Scully, D. Silverman, M. Kendig (Eds.), Electrochemical Impedance: Analysis and Interpretation, ASTM International, West Conshohocken, PA, 1993, doi:10.1520/STP1188-EB.

[38] S. Fajardo, F.R. García-Galván, V. Barranco, J.C. Galván, S.F. Batlle, A critical review of the application of electrochemical techniques for studying corrosion of Mg and Mg alloys: opportunities and challenges, magnesium alloys-selected issue, IntechOpen (2018) http://dx.doi.org/, doi:10.5772/intechopen.79497.

[39] J.A. Yuwono, C.D. Taylor, G.S. Frankel, N. Birbilis, S. Fajardo, Understanding the enhanced rates of hydrogen evolution on dissolving magnesium, Electrochem. Commun. 104 (2019) 106482, doi:10.1016/j.electacta.2015.02.079.

[40] M. Stern, A.L. Geary, Electrochemical polarization: I . A theoretical analysis of the shape of polarization curves, J. Electrochem. Soc. 104 (1957) 56–63, doi:10.1149/1.2428496.

[41] G.J. Brug, A.L.G. van den Eeden, M. Sluyters-Rehbach, J.H. Sluyters, The analysis of electrode impedances complicated by the presence of a constant phase element, J. Electroanal. Chem. Interf. Electrochem. 176 (1984) 275–295, doi:10.1016/S0022-0728(84)80324-1.

[42] S.R. Taylor, E. Gileadi, Physical Interpretation of the Warburg Impedance, Corrosion 51 (1995) 664–671, doi:10.5006/1.3293628.

[43] J.R. Scully, Polarization resistance method for determination of instantaneous corrosion rates, Corrosion 56 (2000) 199–218, doi:10.5006/1.3280536.

[44] C. Ubeda, G. Garces, P. Adeva, I. Llorente, G.S. Frankel, S. Fajardo, The role of the beta-Mg17Al12 phase on the anomalous hydrogen evolution and anodic dissolution of AZ magnesium alloys, Corros. Sci. 165 (2020) 108384, doi:10.1016/j.corsci.2019.108384.

[45] I.B. Singh, M. Singh, S. Das, A comparative corrosion behavior of Mg, AZ31 and AZ91 alloys in 3.5% NaCl solution, J. Magnes. Alloy 3 (2015) 142–148, doi:10.1016/j.jma.2015.02.004.

[46] M.G. Acharya, A.N. Shetty, The corrosion behavior of AZ31 alloy in chloride and sulfate media – a comparative study through electrochemical investigations, J. Magnes. Alloy 7 (2019) 98–112, doi:10.1016/j.jma.2018.09.003.